ORIGINAL RESEARCH

Nanoclay-Doped Electrospun Nanofibers for Tissue Engineering: Investigation on the Structural Modifications in Physiological Environment

Dalila Miele[1], Marco Ruggeri[1], Barbara Vigani[1], Cesar Viseras[2], Francesca Natali[3], Elena Del Favero [4], Silvia Rossi [1], Giuseppina Sandri[1]

[1]Department of Drug Sciences, University of Pavia, Pavia, Italy; [2]Department of Pharmacy and Pharmaceutical Technology, School of Pharmacy, University of Granada, Granada, Spain; [3]Institut Laue-Langevin, Grenoble, France; [4]Department of Medical Biotechnology and Translational Medicine, University of Milano, Segrate Milano, Italy

Correspondence: Giuseppina Sandri, Tel +390382987728, Email giuseppina.sandri@unipv.it

Background: Clay minerals are nanomaterials that have recently been recognized as enabling excipients that can promote cell adhesion, proliferation, and differentiation. When nanoclays are loaded in a 3D polymeric nanostructure, the cell–substrate interaction is enhanced, and other bioactive properties are optimized.
Purpose: In this study, hectorite (HEC)- and montmorillonite (MMT)-doped polymeric scaffolds were explored for the treatment of deep and chronic skin lesions.
Methods: Scaffolds were manufactured by means of electrospinning and then crosslinked by heating. Physicochemical analyses were correlated with in vitro biopharmaceutical characterization to predict the in vivo fate of the clay-doped scaffolds.
Results and Discussion: The addition of MMT or HEC to the polymeric scaffold framework modifies the surface arrangement and, consequently, the potential of the scaffolds to interact with biological proteins. The presence of nanoclays alters the nanofiber morphology and size, and MMT doping increases wettability and protein adhesion. This has an impact on fibroblast behavior in a shorter time since scaffold stiffness facilitates cell adhesion and cell proliferation.
Conclusion: MMT proved to perform better than HEC, and this could be related to its higher hydrophilicity and protein adhesion.
**Keywords:** nanomaterials, montmorillonite, hectorite, chitosan, nanofibers, electrospinning, tissue engineering

Introduction

Clay minerals are historically employed to manufacture both pharmaceutical and cosmetic skin products.[1] Currently, clay minerals have fascinated tissue engineering and regenerative medicine owing to their nanostructures and intrinsic properties that enhance cell attachment, proliferation, and differentiation, along with the antimicrobial activity driven by the high ionic exchange.[2,3] Besides, clay minerals are characterized by the high adsorption capacity of toxic moieties and microorganisms, which makes them suitable for treating skin disorders, such as acne, seborrheic dermatitis, eczema, and psoriasis, while reducing the incidence of local irritations.[4–6] Since the discovery of their bioactivity, several types of clays have been studied, and clay-based medical devices or medicinal products intended to treat deep or chronic skin lesions have been developed.[6–10] Recently, some studies demonstrated the in vivo wound healing effectiveness of natural clays, such as bentonite, halloysite, or hectorite.[11–13] Some findings have demonstrated that clays, especially when coupled in polymeric systems as nanocomposites led to a faster tissue regeneration in terms of enhanced collagen deposition and skin re-epithelialization with negligible scar.[14–16]

Physicochemical interactions with biological fluids play a crucial role in the efficacy of therapeutic platforms in tissue engineering. The bioactivity and, consequently, the in vivo performance are affected and, in certain cases, limited by the

Graphical Abstract
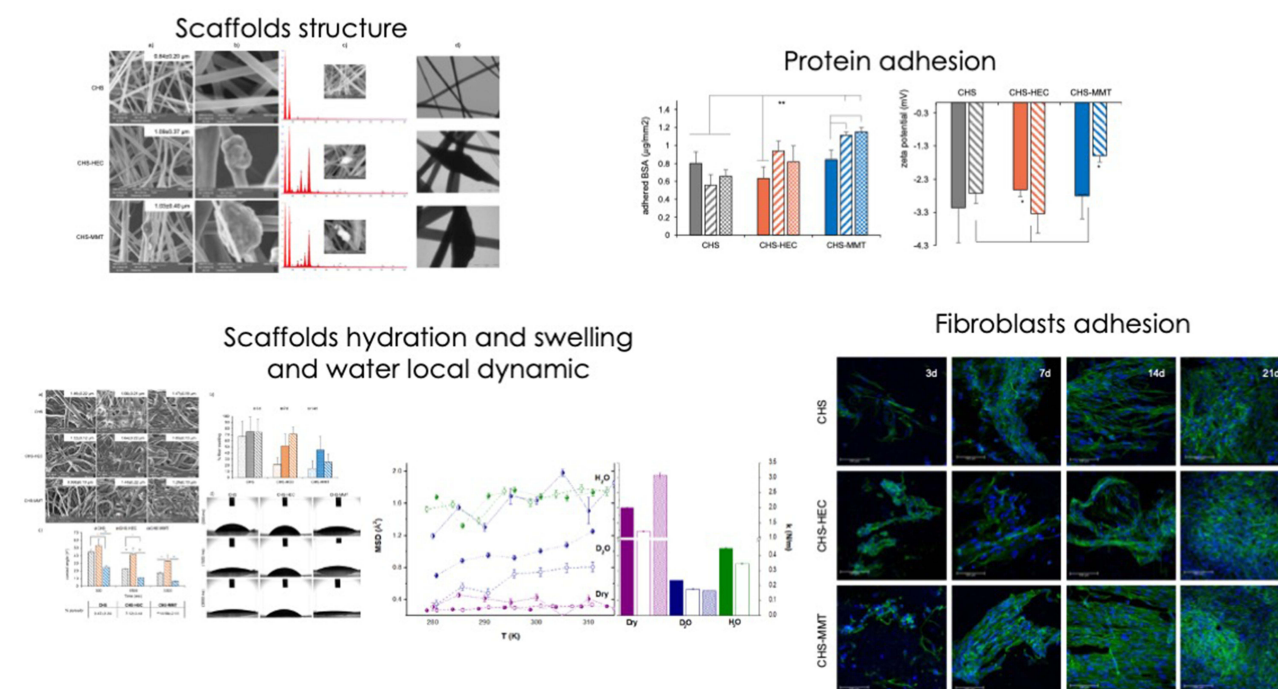
entity and type of the above-mentioned physicochemical interactions.[17] This could induce unexpected reactions and interactions that alter the structure of both biological fluid proteins and the biomedical surface.[18]

Preliminary in vitro physicochemical characterization of the interactions between proteins and scaffolds for tissue engineering as well as scaffold interface transformation following the intimate interaction with extracellular fluids could facilitate a more rational design of medical devices with the desired tissue reactivity and therapeutic potential and to predict their in vivo fate.[19,20]

Given this premise, the purpose of this study was to investigate how the presence of clays in polymeric electrospun 3D scaffolds influences their physicochemical surface properties, particularly their structural and mechanical stability, wettability, and surface charge density in biological/physiological environments. Clay-doped nanofibrous scaffolds based on natural polymers have been manufactured by means of electrospinning due to its versatility.[21,22] Polysaccharides, such as pullulan, chitosan, and chondroitin sulfate, have been selected as scaffold components due to their biodegradability, low immunogenicity, and bioactivity, which resemble the natural extracellular matrix (ECM).[23–25] As shown in our previous study, electrospun chitosan/chondroitin sulfate (CHS) 3D nanofibrers were easily crosslinked using a thermal treatment and were characterized by swelling capacity, biodegradation, and antimicrobial activity.[26] In addition, these scaffolds facilitated cell homing, enhanced cell adhesion and proliferation, and in vivo wound healing.[27] These architectures could offer many advantages including the ability to allow gas exchange between the wound and the surrounding environment, absorption of wound exudates, and enhanced ECM deposition and cellular proliferation, migration, and differentiation. Therefore, this material has been selected as a polymeric nanostructured material for clay doping as enhancers of cell proliferation. In particular, hectorite ($Na_{0.3}(Mg, Li)_3Si_4O_{10}(OH)_2$, HEC) and montmorillonite ($M_x(A_{l2-y} Mg_y) Si_4O_{10}(OH)_2$ nH_2O, MMT), two nanoclay minerals belonging to the smectite group were considered, and their functional properties were compared. Specifically, HEC and MMT are hydrophilic and biocompatible phyllosilicates with planar and lamellar structures, respectively. Two tetrahedral sheets and one octahedral sheet, which together create four anion planes, form the typical 2:1 smectite clay structure.[28,29] More specifically, the two outermost planes are formed by the basal oxygens of the two tetrahedral sheets, whereas the two inner planes are formed

by oxygen atoms shared by the octahedral sheet and the two tetrahedral sheets, as well as hydroxyls from the octahedral sheet. The smectite clays exhibita variable net negative charge that is locally balanced by Na^{2+}, Ca^{2+}, Mg^{2+}, and H^+ located in the interlamellar spaces (galleries). The structure, the chemical composition, the ion-exchange capacity, and the small size of smectite crystals affect their biophysical properties, biocompatibility, antimicrobial properties, and capability to sustain cellular activity during the healing process.[9,30,31] The novelty of this study is related to the doping of natural polymers-based scaffolds with two different nanoclay minerals obtained using a sustainable and green process without solvents and chemical crosslinker. In addition, this study aims to deeply understand how nanocomposites modify the physicochemical and in vitro properties of scaffolds for applications in skin tissue engineering. For this purpose, HEC- or MMT-doped CHS 3D-scaffolds were characterized, and their properties were compared to those of undoped scaffolds. The scaffold morphology was characterized by scanning electron microscopy (SEM) coupled with energy-dispersive X-ray spectroscopy (EDX) and transmission electron microscopy (TEM). The structural properties were investigated spectroscopically using FT-IR (Fourier transform infrared), XRPD (X-ray powder diffraction), small angle X-ray scattering (SAXS), and wide angle X-ray scattering (WAXS), and the surface zeta potential, wettability, and thermal behavior (thermogravimetry (TGA), and differential scanning calorimetry (DSC)) were assessed.

Physicochemical analyses were correlated with in vitro biopharmaceutical characterization to predict the in vivo fate of the clay-doped scaffolds.[32] Considering that CHS scaffolds are conceived as in vivo resorbable therapeutic devices, enzymatic degradation was also assessed. Lysozyme, a macrophage-secreted enzyme that degrades polysaccharides by hydrolyzing the glycosidic bonds in its chemical structure, was used.[33] Moreover, the interaction of the clay-doped CHS scaffold with bovine serum albumin (BSA), as a model protein, was assessed using SEM and Bradford assays.

Proliferation of normal human fibroblasts (NHDF) on doped or undoped CHS scaffolds was also carried out over time to assess biocompatibility. Finally, the cell adhesion and structure were evaluated using confocal fluorescence microscopy.

Materials and Methods

Materials

Polymers: pullulan P (based on maltotriose repeating units, linear α 1–4 and α 1–6 glucan, produced by Aureobasidium pullulans) low MW~200–300 kDa (food grade, Hayashibara, Giusto Faravelli, Italy), chitosan (CHS) (β-(1-4)-linked d-glucosamine and N-acetyl-d-glucosamine) low MW 250 kDa, deacetylation degree 98%, origin fungal was kindly offered by ChitoLytic (Newfoundland, Canada); chondroitin sodium sulfate (CS) (β-1,4-linked D-glucuronic acid and β-1,3-linked N-acetyl galactosamine) bovine 100 EP, low MW 14 kDa, mixture of chondroitin A (chondroitin 4 sulfate) and chondroitin C (chondroitin 6 sulfate) (Bioiberica, Italy).

Clays: hectorite (HEC, 516 ± 15 μm) (Pangel HT-11, TOLSA, Madrid, Spain) and montmorillonite (MMT, 1074 ± 103 μm) (Veegum HS©, TOLSA, Madrid, Spain).

Citric Acid (CA) (monohydrated Citric Acid, EP grade, Carlo Erba, Italy) was used as a crosslinking agent.

Methods

Preparation of Polymeric-Clay Blends

All the polymeric blends were prepared according to the procedures described in a previous work.[26] Briefly, 5%w/w of CHS and CA (in 1:1 molar ratio) were hydrated in acetic acid (90% v/v), then 20% w/w of P enriched with 1%w/w of CS hydrated

Table I Composition (% w/w) of Polymeric Blends Used to Obtain the Clay-Doped Scaffolds

%w/w	PULL	CHS	MMT	HEC	CA	CS	Water/Acetic Acid
CHS	10	2.5			2.5	0.5	55/45
CHS-HEC	10	2.5	2		2.5	0.5	55/45
CHS-MMT	10	2.5		2	2.5	0.5	55/45

in water was added to CHS:CA blend at 1:1 weight ratio. Finally, 2% w/w) clay minerals (HEC or MMT) were added to the blend. Three blends (w/w %) were prepared: CHS, CHS-HEC, and CHS-MMT. The blend compositions are listed in Table 1.

Preparation of Electrospun Scaffolds

Scaffolds were obtained from the CHS, CHS-HEC, and CHS-MMT blends using an electrospinning apparatus (STKIT-40, Linari Engineering, I) equipped with a high-voltage power supply (Razel R99-E 40 kV), a 10 mL syringe with a 21 G needle (0.8×20 mm), and a conductive static collector covered with an aluminum foil. The following parameters were used: ΔV (voltage), 20 kV; needle-to-collector distance, 20 cm; polymer solution flux =0.6 mL/h, spinning time =1 h. The obtained CHS, CHS-HEC, and CHS-MMT scaffolds were then crosslinked and sterilized by heating at 150 °C for 1 h in an oven to avoid their solubilization in biological fluids.[34]

Morphological Analysis

The scaffold morphology was analyzed by SEM (Tescan, Mira3XMU, CISRIC, University of Pavia, Italy) after graphite sputtering. The scaffolds were analyzed after the crosslinking procedure and after 3, 7, and 14 days of hydration in PBS at 37°C. The nanofiber diameters were determined using an image analysis software (Image J, ICY, Institute Pasteur, France). The porosity and swelling of the fibers in PBS were measured using imaging tools (software ImageJ2).

The percentage of fiber swelling overtime was calculated with (Equation 1):

$$\%\text{sw} = \frac{\text{fst} - \text{fs0}}{\text{fs0}} *100 \tag{1}$$

where fs_t is the fiber size at a fixed time and fs_0 is the fiber size in the dry state.

SEM-EDX spectroscopy was performed using a high electron beam (20 kV, 15.8 mm. Images were obtained using a secondary electron detector, and EDX spectra were acquired using an EDAX probe (model Apollo XL 30 mm^2).

Structural Characterization

FT-IR spectra of the samples were obtained using a JASCO 6200 apparatus (USA) equipped with a Ge ATR. All analyses were performed from 400 to 4000 cm^{-1} with a resolution of 1 cm^{-1}, and the results were processed using Spectra Manager v2 software. The FT-IR spectra were smoothed, and noise was removed using the mean movement method.

XRPD analysis was performed using an X-Pert Pro model (Malvern Panalytical, Spain) equipped with a solid-state detector (X-Celerator) and spinning sample holder. The diffractogram patterns were recorded using randomly oriented mounts with CuKα radiation, operating at 45 kV and 40 mA, in the range of 4–70° 2θ. The diffraction data were analyzed using the XPOWDER® software.

Local Dynamics by Elastic Neutron Scattering

For neutron scattering experiments, rectangular dried cuts (3×5 cm^2) of the scaffolds were enclosed in airtight aluminum flat cells of known mass, weighed, and placed in place for measurement. Subsequently, the cuts were extracted from the aluminum cells, carefully dried, desiccated, and fully immersed in D_2O. After draining the excess D_2O, the scaffolds were enclosed again in the original airtight aluminum cells and then weighed and measured. The same procedure was repeated for H_2O-hydration. The hydration level h (h = $g_{water}/g_{scaffold\text{-}dry}$) for all the samples was calculated to be in the range 3.2–3.3.

The samples were then inserted into an aluminum flat sample holder. The elastic neutron scattering (EINS) spectra were recorded using a high-resolution backscattering spectrometer IN13 (Institut Laue-Langevin (ILL), Grenoble, France). With an energy resolution of 8 μeV (full width at half maximum, FWHM) and an accessible momentum transfer range of 0.2 < Q < 4.9 Å−1, IN13 allows the investigation of molecular motions on a timescale up to 100 ps and with an amplitude from 1.3 Å to ~31 Å.

Temperature-dependent scans were recorded for all scaffolds under dry and hydrated D_2O or H_2O conditions. Data were acquired in the temperature range of 278–315 K, above the freezing point of water, to avoid coherent scattering contributions arising from ice Bragg reflections.

The neutron transmission values higher than 85% were chosen in order to optimize the signal-to-noise ratio while keeping low enough the probability of multiple scattering events to be neglected. Also the scattering contributions from

HEC, MMT, and H_2O were estimated and assumed to be 11% from MMT in the CHS-MMT dry compound, and 70% from H_2O in both CHS and CHS-MMT. The standard reduction of raw data (empty scan subtraction, sample transmission correction, and normalization using a vanadium scan) was performed using LAMP Software.[35]

Thermal Analyses

Differential scanning calorimetry (DSC) and thermogravimetric analysis (TGA) were performed using a TGA/DSC1 instrument (Mettler-Toledo GMBH, S), which simultaneously measured mass loss and heat flow in the sample. The analyses were performed in the 25–950°C temperature range and at a heating rate of 10°C/min under atmospheric conditions.

Wettability

The wettability of the electrospun fibers was evaluated using a contact angle meter (DMe-211 Plus) coupled with FAMAS software (Enco, Spinea, Italy). The measurements were performed in a time-based mode to study the variations in contact angle over time. A droplet of water or PBS pH 7.4 was captured for a total time of 3000 ms (every 100 ms, 30 times). A cross-sectional view of the droplet shape was acquired using an instrument CCD camera.

Surface Zeta Potential

The apparent zeta potential (ζ) of each scaffold was determined by measuring the streaming potential (SurPASS 3, Anton Paar GmbH, Austria) using a cylindrical cell. The scaffolds (78 mm^2 active area) were mounted in a dry state on a cylindrical cell. 0.01 M KCl aqueous solution was used as the streaming solvent, and ζ was measured in the pH range of 2–9 to determine the isoelectric point (iep) and ζ at physiological pH.[36–38]

Enzymatic Degradation

Scaffold degradation by lysozyme has also been investigated in vitro. A fixed amount of each scaffold was dipped in 1 mL PBS 0.05 M (pH 6.2) containing 5.7 mg/mL of lysozyme (70,000 UI/mg, Sigma Aldrich, Milan, Italy) at 25°C for 24 h.

The enzyme solution was withdrawn daily, and fresh lysozyme in PBS was added for up to 14 days. Scaffolds dipped in PBS 0.05 M (pH 6.2) without lysozyme were used for comparison.

Glucosamine released after enzymatic activity was assessed using a ninhydrin assay. Briefly, each aliquot in contact with the scaffolds was diluted 1:1 with 1 N perchloric acid and centrifuged at 5000 rpm for 15 min to precipitate and remove lysozyme from the solution.[30] Then, ninhydrin reagent (ninhydrin 2% (w/v), hydrindantin 6.8 mg/L in 3:1 (v/v) DMSO: lithium acetate buffer 4 M, pH 5.2; Sigma–Aldrich, Milan, Italy) was added to each sample at a 1:1 volume ratio under nitrogen atmosphere. Each sample was heated at 100°C for 8 min in a shaking bath. The samples were cooled, vortexed for 15s to eliminate excess hydrindantin, and diluted to 1:10 (v/v) using a 1:1 ethanol/water mixture. The absorbance of each sample was measured at 570 nm (FLUOstar Omega (BMG Labtech, Euroclone SPA, MI, USA). A calibration curve was prepared using glucosamine (concentrations: 0.1, 0.075, 0.05, 0.025, and 0.0125 mg/mL) in phosphate buffer 0.05 M pH 6.2 at 25°C. The calibration curve was linear within the considered range, with R^2 values always higher than 0.995. Then, the scaffolds, subjected to lysozyme activity for 14 days, were dried and analyzed by SEM, as previously described, to investigate the morphology of the nanofibers after enzymatic degradation.

Protein Adsorption

The interaction between the scaffold surface and albumin was evaluated in vitro by protein quantification and zeta potential modification. For protein quantification, 380 mm^2 portions were placed in a 24-well plate and kept in contact with BSA maintaining a protein/fibrous surface ratio of 1.25 $\mu g/mm^2$.

At predetermined times (15, 30, and 60 min), the unadhered BSA was removed, placed in 1.5 mL tubes, frozen at −40°C, and lyophilized for 24 h (Heto 15, Analitica De Mori, Italy). Lyophilized samples were resuspended in 0.1 mL of distilled water and vortexed, and BSA was quantified using the Bradford assay in a 96-well plate. At this purpose, 200 μL of Bradford reagent was added to each sample, and after 5 min of incubation, the signal was read at 595 nm using a FLUOstar Omega UV/Vis spectrophotometer (BMG Labtech, Euroclone SPA, Milan, Italy). A calibration curve was prepared using BSA in PBS (pH 7.4), range from 0.1 to 1.4 mg/mL . The calibration curve was linear within the considered range, with R^2 values always higher than 0.995.

The amount of BSA adhered to the scaffolds was calculated and expressed in μ grams of protein adhered per mm^2. The protein residues that adhered to the fibrous scaffolds were imaged using SEM, as previously described.

For the surface zeta potentials, the scaffolds were kept in contact with BSA at a protein/fibrous surface ratio of 1.25 μg/mm^2. Subsequently, surface ζ was measured at pH 7.4, as previously described.

Biocompatibility and Adhesion of Normal Human Dermal Fibroblasts (NHDFs)

The cytocompatibility of the undoped and doped scaffolds was evaluated using an AlamarBlue $^®$ assay. Normal human dermal fibroblast cells (NHDFs from juvenile foreskin, PromoCell, WVR, Italy) were cultured in DMEM medium (Sigma-Aldrich, Italy) supplemented with 200 IU/mL penicillin/0.2 mg/mL (growth medium, GM) (Sigma-Aldrich, Italy) and with 10% v/v foetal bovine serum (FBS, Sigma, Italy). Briefly, scaffolds were cut into 1.9 cm^2 pieces and placed in a 24-well plate. Then, 5×10^4 cells were seeded onto the scaffold surface and cultured for 3, 7, 14, and 21 d. Cells grown at the bottom of the wells were used as controls (GM). At each time point, cell viability was assessed using AlamarBlue $^®$. Briefly, 100 μL of 10% (v/v) AlamaBlue$^®$ in DMEM was added to each well. After 3 h, fluorescence was measured (λex 530 nm and λem 560 nm) using a FLUOstar Omega UV/vis spectrometer (multi-mode microplate reader, BMG Labtech, Euroclone SPA, Milan, Italy). Cell viability was expressed as fluorescence intensity and compared to cells grown under standard conditions (GM).

Confocal microscopy (CLSM) was used to visualize NHDF adhesion to the scaffolds and cell morphology. Briefly, at each timepoint of the biocompatibility test, the cells were fixed for 1 h at room temperature using 3% v/v of glutaraldehyde and then washed twice with PBS for 5 min. The substrates were permeabilized with 0.1% w/w of Triton x-100 solution for 5 min, washed twice, and treated with 50 μL of 25 μg/mL FITC-phalloidin (Sigma Aldrich, Milan, Italy), to avoid light exposure. After 40 min, the cells were washed twice in PBS, and the cell nuclei were stained with 100 μL of 0.5 μg/mL Hoechst 33,258 (Sigma Aldrich, Milan, Italy) for 10 min. Finally, the substrates were washed twice for 5 min, and the samples were placed on a microscope slide and analyzed by CLSM (Leica TCS SP5, Leica Microsystems, Milan, Italy) at λex = 346 nm and λem= 460 nm for Hoechst 33,258 and λex = 496 nm and λem = 516 nm for FITC phalloidin. The acquired images were processed using the LASX software (LASX Leica Microsystem, Italy).

# Results and Discussion
Chemico-Physical Characterization
SEM, EDX, FT-IR

SEM and TEM micrographs of the electrospun scaffolds after the crosslinking process before and after 7 days of hydration are shown in Figure 1. From the undoped blends, homogeneous fibers with no evident defects were collected, while MMT or HEC doping caused roughness on the fiber surface, conceivably related to the entrapment of clay particles into the polymeric matrix. At a higher magnification (25 kx), the fibers appeared broadened with bulges attributable to inorganic particles (Figure 1c), as previously described in the literature.[32] The clay doping caused a slight but not statistically significant increase in the fiber diameter compared to the undoped fibers, independent of the clay type. In both cases, the diameter of the clay-doped fibers was 1 μm, which was higher than that of the undoped fibers (0.8 μm). However, fiber morphology was not affected by 7-days of hydration in PBS, although a statistical increase in fiber size was recorded in all scaffolds due to a slight swelling. This is much more considerable for undoped fibers that increase their size by approximately 43%, while it is less substantial for doped fibers and equal to 20% and 17% for HEC and MMT, respectively. This could be attributed to the clay minerals acting as water traps in the clay galleries, impairing the free hydration of the polymeric matrix.

The elemental composition confirms that the bulges in the doped fibers are made of clay because the signals of all the smectite elements are present (Si, Mg, Al, Fe, and K) and F is present only in HEC-CHS, confirming the clay identity.

The fiber porosities of the undoped (9.47±2.24%) and HEC-doped (7.12±3.44%) fibers were not significantly different, whereas the porosity was significantly higher for MMT-doped (13.56±2.13%) fibers, which could be related to the MMT particle size that is 2 folds higher than that of HEC.

Figure 2a shows the FTIR profiles of the scaffolds and their pristine components for comparison. The peaks are in agreement with the current literature, where the specific assignments are given.[39,40] In particular, the profiles suggest that
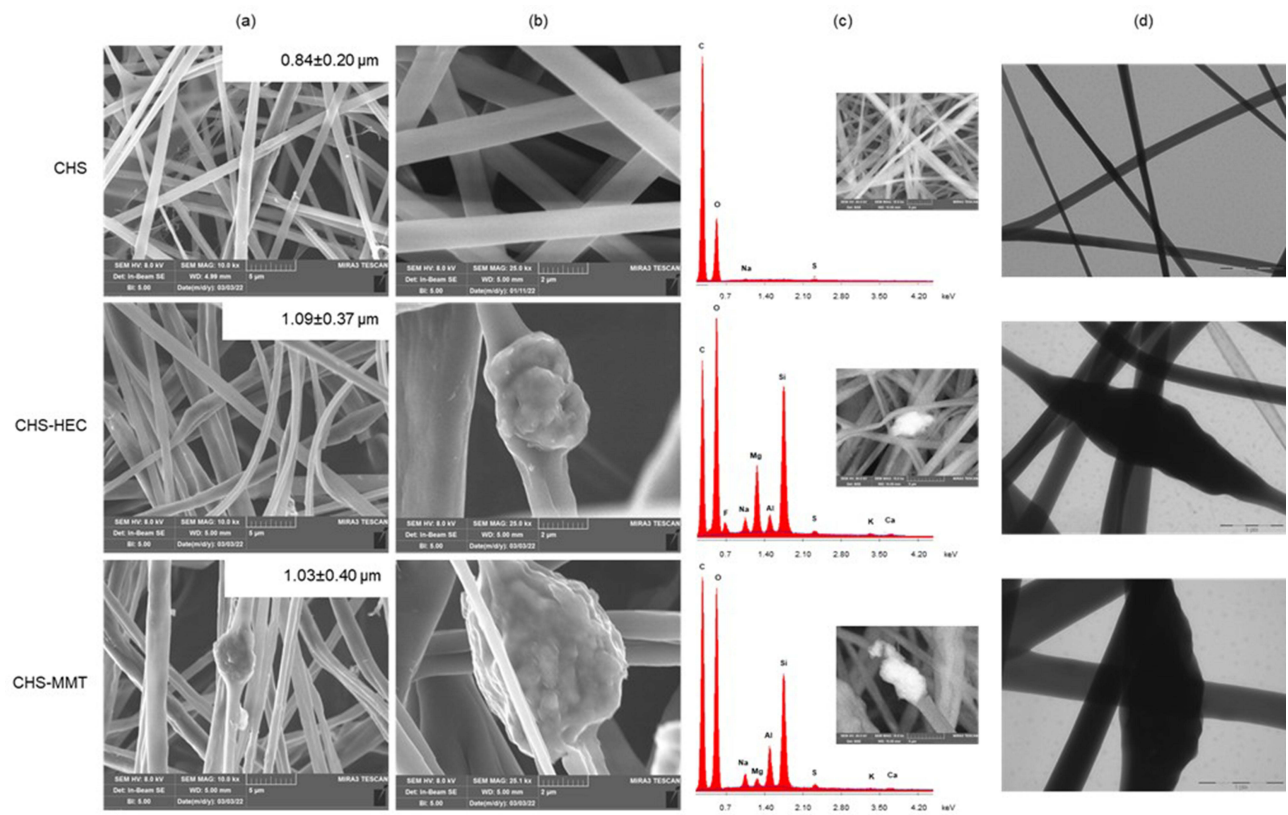
Figure 1 Undoped (CHS) and doped scaffolds with hectorite (CHS-HEC) or montmorillonite (CHS-MMT): (**a**) SEM micrographs of nanofibers (mag. 10kx). In the inset the fiber diameters are reported; (**b**) SEM micrographs of nanofibers (mag. 25kx); PBS; (**c**) SEM- EDX spectra (mag. 25kx); (**d**) TEM micrographs (scale bar 2 μm in CHS and 1 μm in clay-doped fibers).
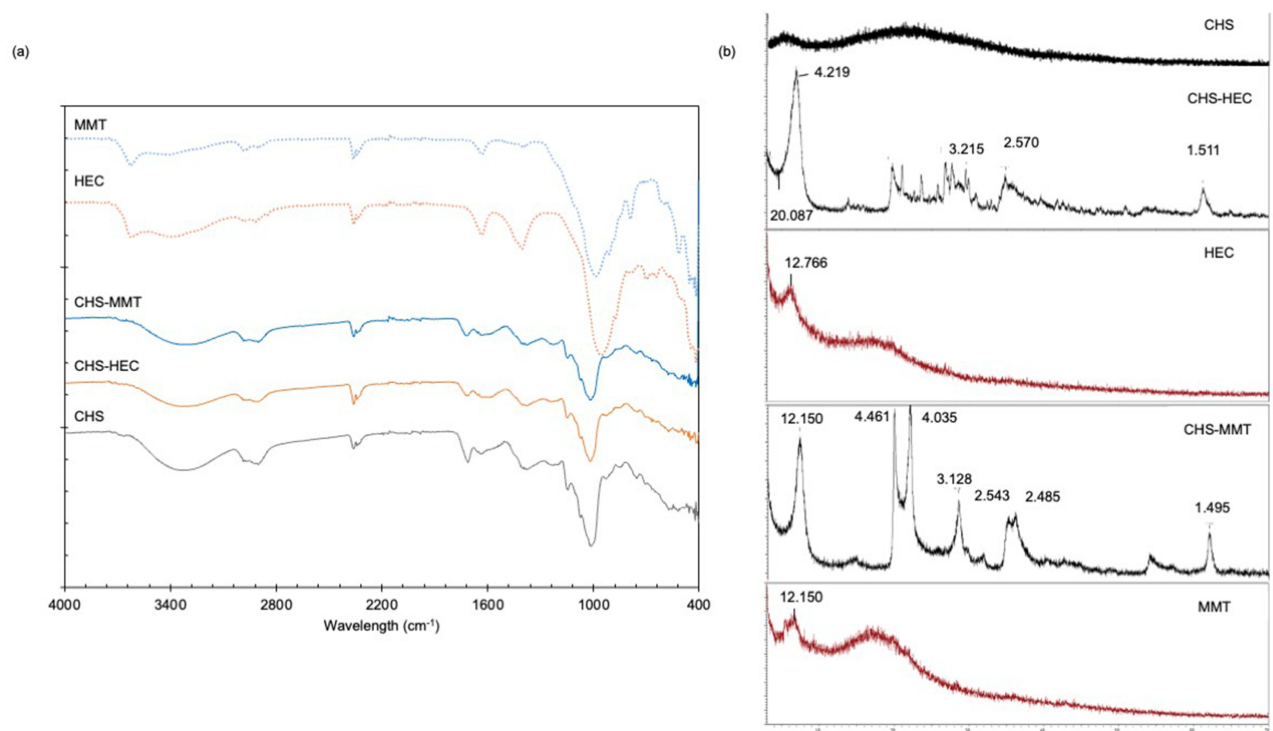
Figure 2 FT-IR (**a**) and XRPD (**b**) spectra of undoped (CHS), hectorite-doped (CHS-HEC) and montmorillonite-doped (CHS-MMT) scaffolds. The spectra are compared to pristine hectorite (HEC) and montmorillonite (MMT).

there is a slight shift in the region of the amide I band at 1640 cm^{-1}, conceivably caused by the interaction between CHS and CA. This is largely prevented by the presence of anionic groups in CS (sulfate) and the steric hindrance of the polymer, which prevents massive covalent bond formation.[30] The interaction between CHS and CA allowed to consolidate the 3D structure and no solubilization of the scaffold occurred, while maintaining the swelling capacity of the scaffolds as previously observed in the SEM analysis.

Moreover, the pristine HEC showed characteristic peaks at 654 cm^{-1} attributable to OH bending, Si-O stretching at 1042 cm^{-1}, Si-O out-of-plane bending at 701 cm^{-1} and Si-O in-plane bending at 467 cm^{-1}. These are partially shifted at lower wavelength numbers, probably due to the water moieties retained in the lamellar structure.[41] The HEC doping is not particularly evident in HEC-doped scaffolds because the HEC characteristic peaks are partially hidden by the polymeric matrix. Despite this, a shift of the Si-O stretching band from 957 cm^{-1} to 1010 cm^{-1} was recorded, which is ascribable to the interactions between the clay-polymeric chains, which become stronger after thermal treatment, probably causing water displacement.

Similarly, pristine MMT showed characteristic absorption bands, particularly the OH-stretching vibrations at 3624 cm^{-1}, and the bending vibrations of AlAlOH and AlMgOH at 916 and 840 cm^{-1}, respectively, while the stretching vibrations of the Si–O groups at 986 cm^{-1} slightly shifted from 1040 cm^{-1} owing to clay hydration. The bands at 523 and 470 cm^{-1} related to the Al–O–Si and Si–O–Si bending vibrations, respectively, were also visible, together with the bending vibrations at 625 cm^{-1} assigned to the Al–O and Si–O pairs. Moreover, water stretching and bending vibrations were recorded in the ranges of 3420–3450 cm^{-1} and 1635 cm^{-1}, respectively.[42,43]

Similar to CHS-HEC, CHS-MMT showed characteristic bands of MMT partially hidden by the polymeric matrix (Figure 2a). MMT hydration caused slight shifts in the water stretching and bending vibrations at 3400 cm^{-1} and 1632 cm^{-1} together with peak fading. Furthermore, the typical stretching vibrations of the Si–O groups at 986 cm^{-1} shifted to higher wavenumbers, indicating a possible polymer–clay interaction.

Structural Characterization

Figure 2b shows the XRPD spectra of the HEC and MMT scaffolds compared with those of pristine HEC and MMT. The CHS scaffold was characterized by an amorphous pattern, and no crystalline or paracrystalline behavior was observed. The patterns of pristine HEC and MMT are characterized by peaks at 12.776 and 12.150 2θ, respectively, which correspond to the distance of the d001 basal reflection determined by the galleries equal to 6.9 Å and 7.3 Å, respectively. In the CHS-HEC and CHS-MMT scaffolds, d001 basal reflections were present, and no shift occurred, indicating that gallery heights were preserved. It is conceivable that polymer intercalation into the clay galleries does not occur, and this is probably due to the greater amount of anionic or neutral moieties in the polymeric blends, which are conceivably unable to displace the counter cations in the interlayer space, preventing interaction with the negatively charged clay sheets.

Local Dynamics

The local dynamics of macromolecules within scaffolds modulate their stiffness, which influences the mechanics of cell growth. The local mobility was investigated using an elastic neutron scattering technique.

In Figure 3 (left panel), the Mean Square Displacements (MSD) calculated from the slope in the low-q region of the semi-logarithmic plot of the elastic neutron scattering intensity, S(q, ω = 0), collected at different momentum transfers q, are reported for the CHS, CHS-HEC, and CHS-MTT scaffolds.[44,45]

The temperature variation of MSDs can be interpreted in terms of an empirical effective force constant <k>, called resilience.[46] It describes the rigidity or resilience of macromolecules. The effective average force constant <k>, calculated from the slope of the MSD as a function of temperature, is shown in Figure 3 (right panel).

The local dynamics in all the systems were clearly enhanced upon H$_2$O or D$_2$O hydration with respect to the corresponding dry states. In the dry scaffolds, the MSD values were very low, and the addition of MMT or HEC did not induce significant differences. This is also reflected in the k histogram, where much higher force constants are found for the dry samples with respect to the H$_2$O and D$_2$O hydrated samples, indicating a higher stiffness.

In the H$_2$O hydrated samples, the high scattering contribution from water eventually hides any changes in the scaffold dynamics upon the addition of MMT (similar MSD values) or HEC (scattered MSD values), even though only confined
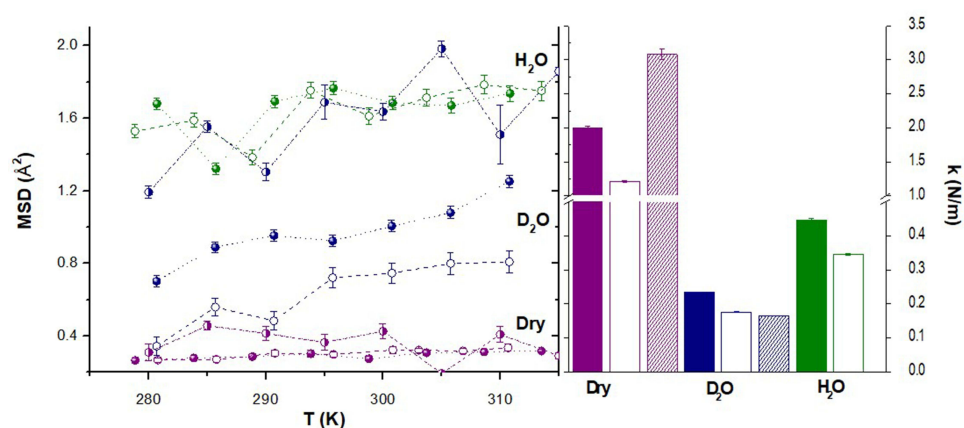
Figure 3 MSD (left panel) and force constants (right panel) calculated for CHS (filled symbols/columns), CHS-HEC (pattern symbols/columns), and CHS-MMT (empty symbols/columns). Purple= dry scaffolds; Blue: samples hydrated in D_2O; Green = samples hydrated in H_2O.

or partially bounded water molecules with retarded dynamics may be visible on IN13, given its energy resolution, in which the free water contribution appears as a flat background.

A clear difference was observed in the D_2O hydrated samples, in which the contribution of water was hidden owing to H–D isotope exchange. The relatively low scattering contribution from MMT and HEC with respect to the matrix (CHS), of 10–11%, allows to safely state that the addition of MMT or HEC clay affects the overall scaffold local dynamics, thus suggesting a quite distribution of clays within the fibers.

The addition of HEC clay enhanced the local dynamics of CHS-HEC, with high MSD values and a lower force constant, indicating a softening effect. The presence of MMT also lowered the force constant; rather, the MSDs did not change accordingly, being lower than those of the native scaffolds. This result suggests the confinement of the local mobility without a stiffening effect. Smectic clays are characterized by stacked lamellae (platelets) with interlayer spacing, where solvent molecules can penetrate during hydration. The swelling behavior depends on the interlayer cations.[47] Considering this, the results show that under hydrated conditions, both the amplitude of the local mobility of molecular groups within the scaffolds and their resilience are dramatically affected, resulting in a lower stiffness at the nanoscale. Doping deeply influences the scaffold softness, further decreasing their stiffness. This plays a role in cell anchoring and adhesion to the scaffold because they experience substrate mechanical properties at the nanoscale, which in turn influence their growth and proliferation.

Thermal Analyses

The DSC and TGA spectra of the pristine components are shown in Figure S1. Specifically, HEC and MMT weight loss induced by heating was defined between 5 and 15% of the weight in the region from 140 to 576°C, corresponding to the loss of the water confined between the clay platelets (layers). Dihydroxylation of clays usually occurs at higher temperatures (around 580 and 687°C) and accounts for 1.6% of the mass loss.[47,48] Both pullulan and chitosan showed weight loss in three stages, with total carbonization at 560°C and 600°C, respectively. Chondroitin sulfate thermal degradation profile showed the first weight loss at approximately 100°C assigned to evaporation of water (19% loss in weight) followed by an intense weight loss with maximum rate at 507°C, corresponding to depolymerization of the polysaccharide, and carboxylate and sulfate group degradation. In addition, the thermogram showed similar final residues of approximately 21%, which could be related to carbon residues. Citric acid also showed a small weight loss owing to the water evaporation and an intense weight loss at 220°C.

The TGA spectra of the scaffolds (CHS, CHS-HEC, and CHS-MMT) are shown in Figure 4. In general, all the scaffolds are characterized by a first weight loss step at around 100°C, corresponding to the water evaporation, followed by a two-stage degradation at temperatures higher than 200°C. As for DSC analysis, the scaffolds presented a first broad peak (40–100°C) corresponding to the water evaporation. At temperatures higher than 200°C, other endothermic peaks appeared, corresponding to component degradation. In general, independent of the composition, thermal analysis suggested that the scaffolds were stable in the temperature range used during the crosslinking process.

The TGA profiles showed that the clay loading was not significantly different from the theoretical (11.76%).
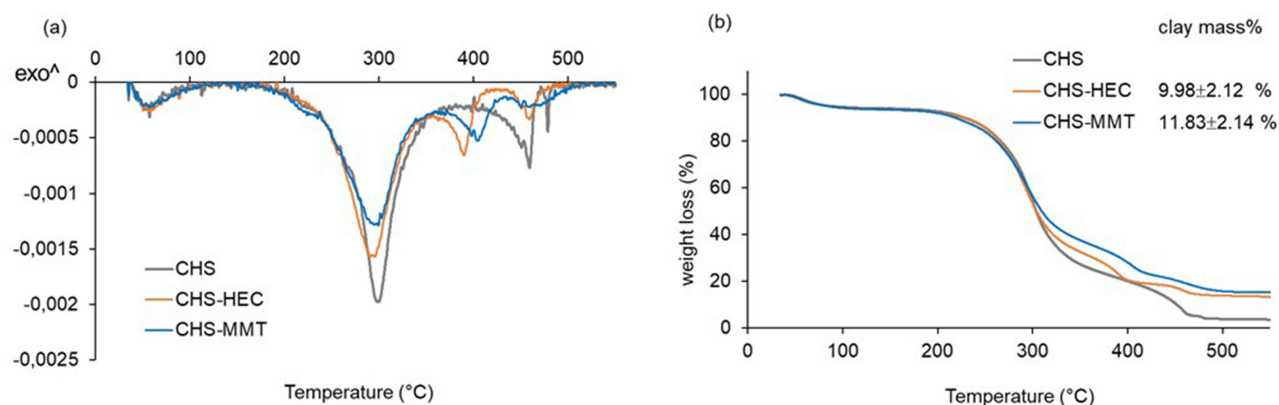
Figure 4 DSC spectra (**a**) and TGA spectra (**b**) of undoped (CHS), hectorite-doped (CHS-HEC) and montmorillonite-doped (CHS-MMT) scaffolds. The inset shows the % of mass residues that correspond to the clay loaded.

Wettability

The morphology of hydrated scaffolds has been investigated and the fiber swelling (%) calculated (Figure 5a and b). Scaffold hydration caused a significant increase in fiber dimensions. In CHS scaffold, fiber swelling occurred after 3 days hydration with a 70% increase in diameter, and the fiber aspect remained unchanged up to 14 d, suggesting a strong stability. The doped scaffold seems less sensitive to hydration with a shorter change in fiber dimensions, and in any case, HEC doping causes a linear increase in fiber diameters upon hydration over time up to 14 days, whereas MMT doping allows the fiber dimension to be maintained over time. These behaviors are probably related to the different degrees of
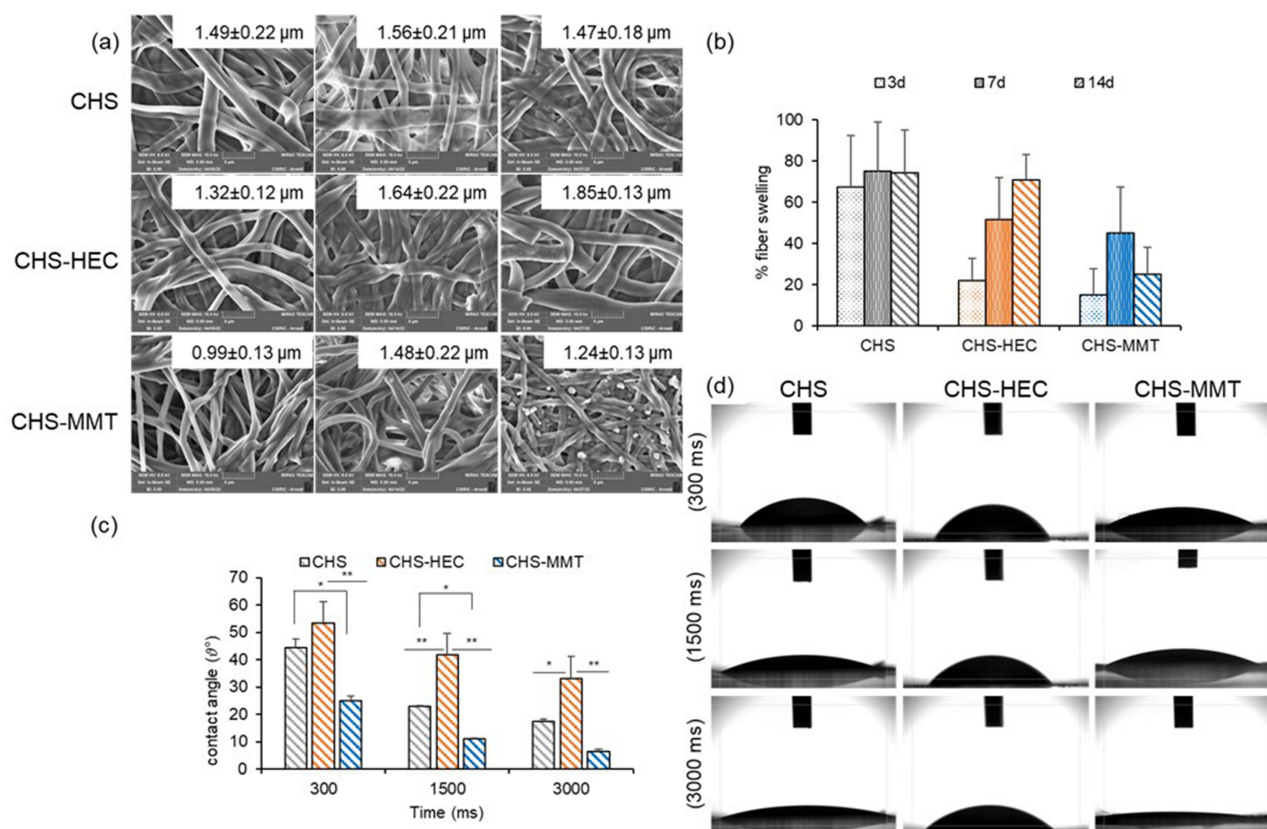
Figure 5 (**a**) SEM micrographs of the scaffolds after hydration in water; (**b**) fiber swelling (mean values ± s.d.; n=4%); (**c**) contact angles (θ°) vs times in water; (**d**) digital images, after 300 ms, 1500 ms and 3000 ms from the water droplet-release on the undoped (CHS), hectorite-doped (CHS-HEC) and montmorillonite-doped scaffolds (CHS-MMT) (1-way Anova, post hoc Scheffè test (mean values ± s.d.; n=4; *p<0.05 **p<0.01).

hydrophilicity of the two clays; MMT, which is more hydrophilic, seems to be able to accommodate a higher amount of water molecules between layers, resulting in less transfer with the polymeric matrix.

Contact angle measurements were performed to investigate the wettability of the scaffolds in water (Figure 5c and d). The presence of MMT and HEC clays had opposite effects on the wettability of the scaffolds. Doping with MMT enhances wettability, whereas doping with HEC results in less wettable scaffolds. This behavior is in agreement with wettability studies on clays reported in the literature. The contact angle between water droplets and clays has been found to be approximately 25° for MMT,[49] whereas it has been found to be greater (approximately 58° for Hectorite).[50] Remarkably, the contact angles measured for water droplets on doped scaffolds at short times are similar to those reported for clays, suggesting a strong modulation of the surface properties by MMT (more hydrophilic) and HEC (less hydrophilic). The different effects on wettability also persisted for longer times when water partially penetrated the scaffolds.

Surface Zeta Potential

The surface zeta potential (ζ) of the scaffolds was investigated as a function of pH using the surface streaming potential. These results are consistent with the literature[21] and show a decrease in ζ values with increasing pH, caused by the pKa of chitosan amino groups that have an alkaline character (Figure 6). A similar behavior was observed for the HEC-doped scaffolds. Clay doping minimally influences the zeta potential, and all the scaffolds have been characterized by a IEP close to 3;[51] moreover, the zeta potential at pH close to that of the extracellular fluid (7.4) (lesions) was slightly negative for all scaffolds (Figure 7b).[52,53] All scaffolds have a negative zeta potential in physiological fluids, stemming from an interaction between the sulfate groups of CS and the amino groups of CHS that compete with the interaction between CHS and CA (1:1 weight ratio to chitosan).

## Biopharmaceutical Characterization

Enzymatic Degradation

Scaffold degradation by lysozyme was investigated by monitoring the release of glucosamine, the product of the enzymatic reaction, and fiber morphology upon degradation (Figure 7). CHS and CHS-HEC were characterized by similar degradation profiles for up to 10 days (Figure 7a). For a longer time, CHS-HEC was characterized by a lower profile, which agrees with the lower hydrophilicity (higher contact angle) that could delay the enzymatic reaction.

CHS-MMT exhibited a higher degradation profile over time. As previously reported by Faccendini et al, the electrostatic interaction due to the positively charged chitosan amino groups and the negatively charged sulfate groups of chondroitin sulfate confers superior resistance to enzyme degradation, preventing the scaffold-lysozyme interaction.[30] This alters the enzyme activity causing alterations in fiber morphology (Figure 7b) and the changes are particularly
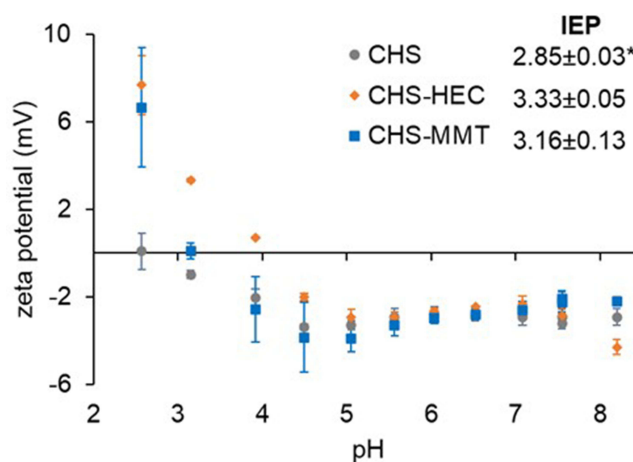
Figure 6 Zeta potentials ζ(mV) of undoped (CHS) or hectorite (CHS-HEC) or montmorillonite (CHS-MMT) doped scaffolds over a pH range of 2 to 9; the inset shows the isoelectric point values (IEP) of the 3 different formulations (1-way Anova, post hoc Scheffè *p<0.05; mean values ± s.d.; n=3).
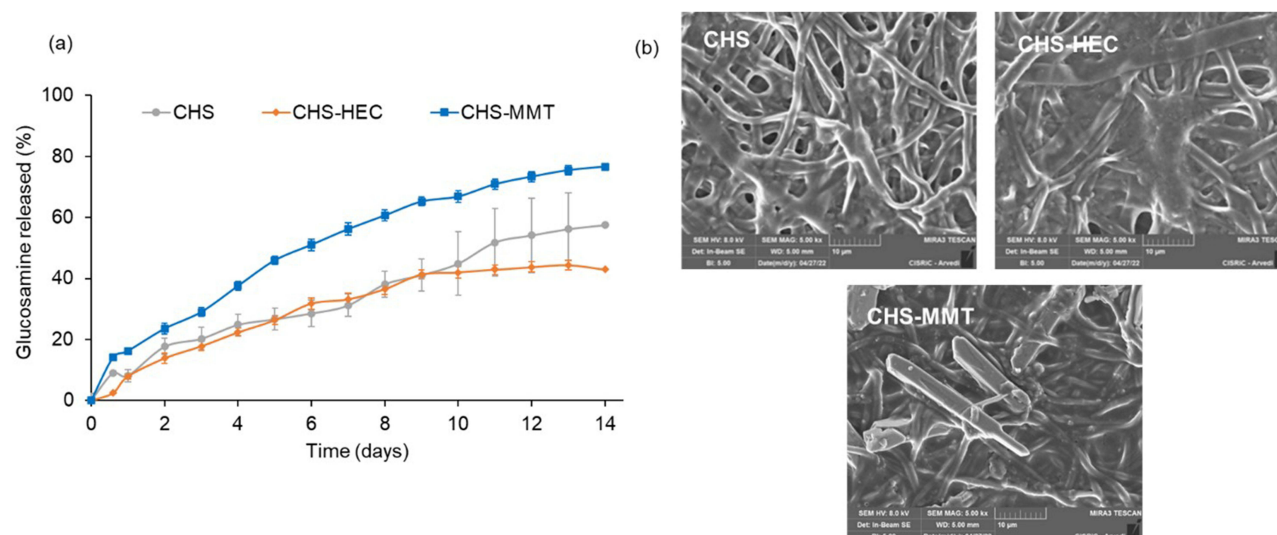
Figure 7 % Glucosamine released by the time (mean values ± s.d.; n=4) (**a**); SEM micrographs of scaffolds after 14 day of lysozyme degradation (**b**): CHS; CHS-HEC; CHS-MMT.

evident when MMT is doped. The fibers appeared broken at multiple points after 14 d of contact, and although the nanofibrous structure was preserved, this indicated that lysozyme caused structural degradation.

Protein Adsorption

Protein adsorption is a crucial factor for the effectiveness of scaffolds intended for tissue regeneration. In fact, serum proteins and extracellular proteins promote scaffold biocompatibility and positively affect cell adhesion, proliferation, and differentiation.[54] Protein adsorption in vivo is a complex and dynamic process with noncovalent interactions, including hydrogen bonding, electrostatic forces, hydrophobic interactions, and van der Waals forces. In vivo, the type, amount, and conformation/orientation of adsorbed proteins are guided by the implant surface properties, including surface morphology, wettability, and surface charges. Protein adsorption onto an implant surface consists of an adsorption sequence of competitive proteins: low-molecular-weight proteins are the first interacting proteins and are generally replaced by high-molecular-weight proteins. Albumin is the most abundant physiological protein and one of the most absorbed proteins.

Figure 8a reports the albumin (BSA) adsorbed onto the scaffolds. The albumin adsorption seems strictly related to the hydrophilicity/hydrophobicity of the surface considered and it is reported that nanostructure facilitates it. The results are in agreement with the wettability findings and the higher hydrophilicity of MMT conceivably promotes the albumin interaction.[55,56] Despite the negative zeta potential at pH 7.4, all the scaffolds are able to establish non-ionic interaction
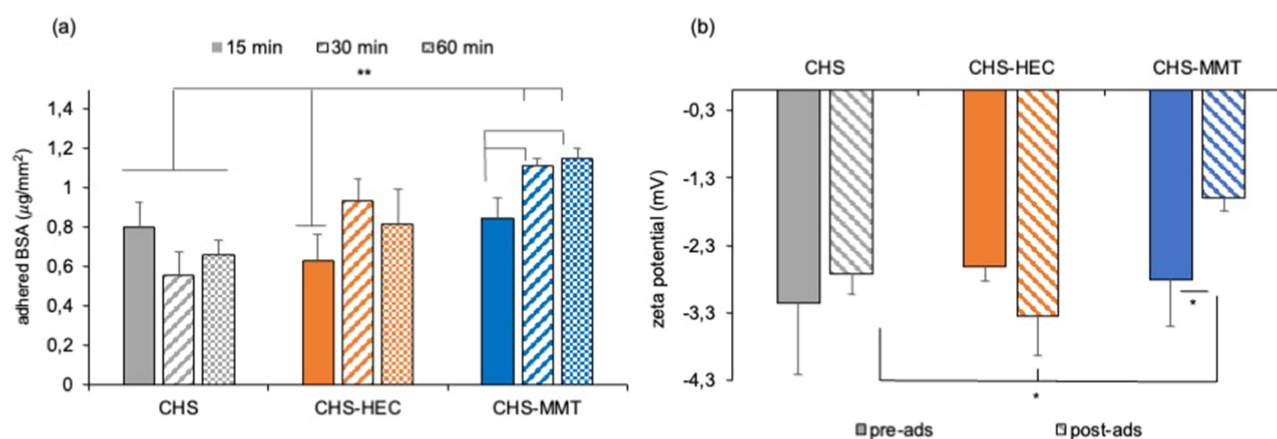
Figure 8 (**a**) μg of protein per mm^2 of scaffold adhered after 15, 30 and 60 minutes. 1-way Anova – Test W-test *p<0.01 (mean values ± s.d.; n=4); (**b**) zeta potential (mV) at pH 7.4 before (pre-ads) and after 60 minutes of contact with BSA (post-ads), of undoped (CHS), hectorite-doped (CHS-HEC) or montmorillonite-doped (CHS-MMT) scaffolds.1-way Anova -post hoc Scheffè test *p<0.01 (mean values ± s.d.; n = 4).

with albumin (pKa 5) that is negatively charged at pH 7.4 and less prone to electrostatically interact with nanofibrous structures. In fact, it has to be considered that the electrostatic interaction is not the only mechanism and other weak bonds could be involved supporting the interaction of albumin with the scaffolds.

CHS doping with HEC did not significantly change the albumin adsorption, and the scaffold zeta potentials remained almost the same (Figure 8b). In contrast, MMT doping caused a significantly higher adsorption of albumin and a significant increase in zeta potential with respect to the native scaffolds and other scaffolds after protein adsorption, acquiring the zeta potential typical of the plasmatic proteins in physiological environments.

Adhesion of Normal Human Dermal Fibroblasts (NHDFs) Onto Scaffolds

The scaffold surface charge, protein adhesion, and nanostructured morphology have been reported as key factors affecting cell adhesion and proliferation.[57,58] Normal human fibroblasts show high proliferation up to 21 days, which was not significantly different from the standard growth condition (GM growth medium), suggesting that scaffolds were a suitable substrate for sustaining fibroblast proliferation over time (Figure 9). However, the confocal images showed faster fibroblast adhesion and
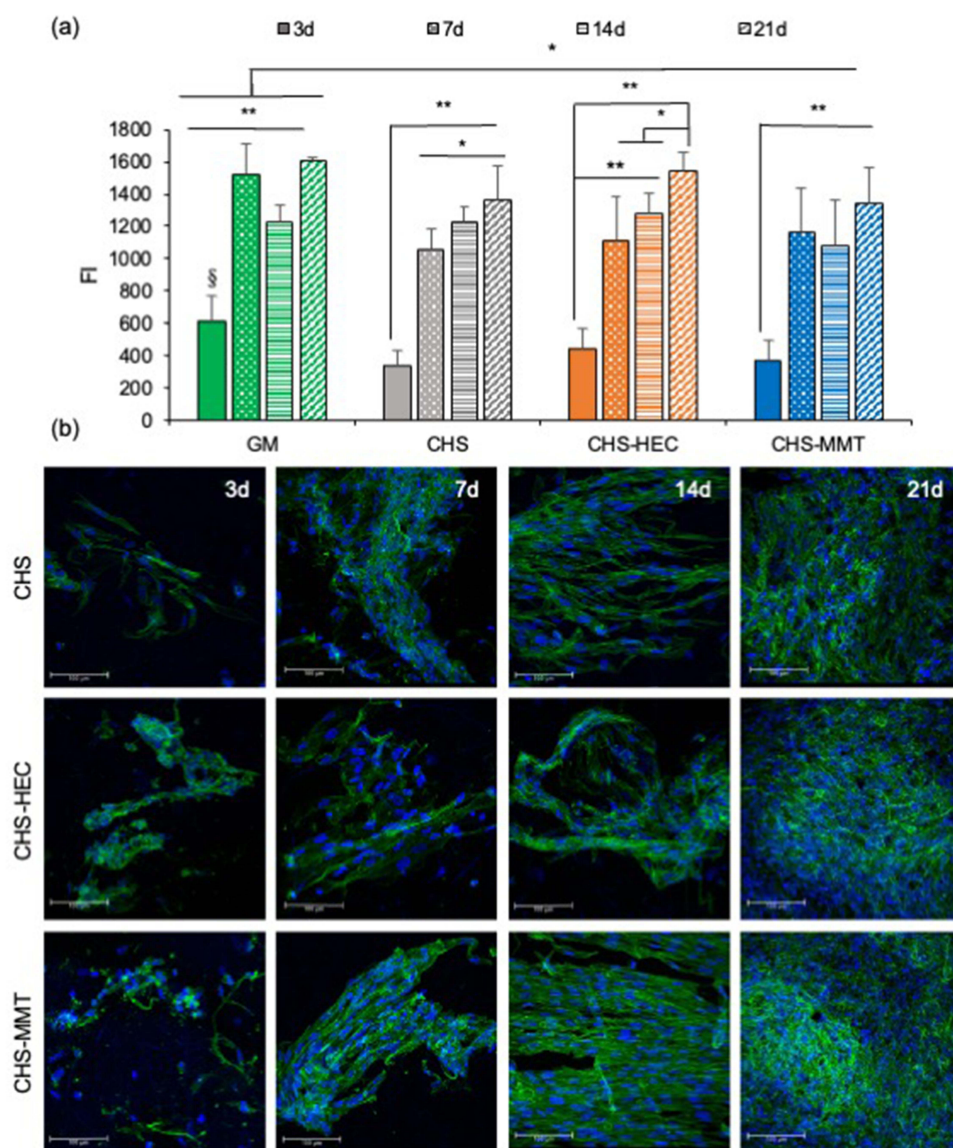
Figure 9 Fluorescence intensities (FI) of reduced alamarblue® (**a**) and CLSM micrographs (**b**) after 3, 7, 14 and 21 days of culture of normal human dermal fibroblasts (NHDF) onto undoped scaffolds (CHS) and doped with clays: hectorite (CHS-HEC) or montmorillonite (CHS-MMT). NHDF grown onto the bottom of the well were considered as control (GM) (mean values ± s.d.; n = 8; 1-way Anova, MRT test, **p<0.01; *p<0.05).

proliferation on CHS-MMT scaffolds. After 14 days, fibroblasts completely covered the scaffold surface and were characterized by a fusiform shape and good alignment, resembling cell organization following dermal collagen bundles.

After 21 days, the fibroblasts grown on the scaffolds appeared confluent, independent of clay doping and the type of clay used.

It seems that the fibroblast behavior is deeply influenced by nanoclays in a shorter time, probably because of the nanoclay's capability to tune system swelling, whereas in a prolonged time, the polymeric matrix induces a higher impact. MMT increases the stiffness of the polymeric matrix, whereas HEC determines the softness of the scaffold. Scaffold stiffness facilitates cell adhesion and proliferation. This plays a role in cell anchoring and adhesion to the scaffold because they experience substrate mechanical properties at the nanoscale, which in turn influence their growth and proliferation.[59] The better performance owing to MMT doping could also be related to the high wettability and protein adhesion.

Conclusion

Chitosan/glycosaminoglycan scaffolds were successfully doped with hectorite or montmorillonite to study how the presence of an inorganic nanomaterial could affect scaffold behavior from both physicochemical and preclinical points of view. The presence of nanoclays alters the nanofiber morphology and size, and MMT doping increases wettability and protein adhesion. Moreover, nanoclay doping influences the swelling and mechanical behavior of the systems and, while MMT increases the system stiffness, HEC causes softening. This has an impact on fibroblast behavior in a shorter time since scaffold stiffness facilitates cell adhesion and cell proliferation. For this reason, MMT proved to perform better than HEC, which could also be related to its higher hydrophilicity and protein adhesion. Nanoclays are stable into the 3D structures as demonstrated by thermal analysis. Although clays are not biodegradable, their safe profile has been reported by several studies. In fact, there are a few evidence in the literature that show excellent safety without foreign body rejection upon system degradation in vivo. It could be supposed that clay particles are mechanically removed during skin layers regeneration from the wound bed to the epidermal layer.

Although further studies are needed to clarify the in vivo system impact, nanoclay doping proved to be effective in tuning the system performance.

Acknowledgments

Disclosure

The authors report no conflicts of interest in this work.

References

1. López-Galindo A, Viseras C, Cerezo P. Compositional, technical and safety specifications of clays to be used as pharmaceutical and cosmetic products. *Appl Clay Sci*. 2007;36:51–63. doi:10.1016/j.clay.2006.06.016
2. Naumenko EA, Guryanov ID, Yendluri R, Lvov YM, Fakhrullin RF. Clay nanotube–biopolymer composite scaffolds for tissue engineering. *Nanoscale*. 2016;8:7257–7271. doi:10.1039/C6NR00641H
3. Mousa M, Evans ND, Oreffo ROC, Dawson JI. Clay nanoparticles for regenerative medicine and bio-material design: a review of clay bioactivity. *Biomaterials*. 2018;159:204–214. doi:10.1016/j.biomaterials.2017.12.024
4. Gaharwar AK, Cross LM, Peak CW, et al. Nanoclay for bio-medical applications: regenerative medicine, therapeutic delivery, and additive manufacturing. *Adv Mater*. 2019;31:1900332. doi:10.1002/adma.201900332
5. Cervini-Silva J, Ramírez-Apan MT, Gómez-Vidales V, Palacios E, Montoya A, De Jesús ER. Anti-inflammatory, anti-bacterial, and cytotoxic activity of fibrous clays. *Colloids Surf B*. 2015;129:1–6. doi:10.1016/j.colsurfb.2015.03.019
6. Carretero MI, Gomes CSF, Tateo F. Clays, drugs, and human health. *In Develop Clay Sci*. 2013;5:711–764.
7. Ghadiri M, Hau H, Chrzanowski W, Agus H, Rohanizadeh R. Laponite clay as a carrier for in situ delivery of tetracycline. *RSC Advan*. 2013;3:20193–20201. doi:10.1039/c3ra43217c
8. Tenci M, Rossi S, Aguzzi C, et al. Carvacrol/clay hybrids loaded into in situ gelling films. *Int J Pharm*. 2017;31:676–688.
9. Viseras C, Carazo E, Borrego-Sánchez A, et al. Clay minerals in skin drug delivery. *Clays Clay Miner*. 2019;67:59–71.
10. García-Villén F, Souza I, de Melo Barbosa R, et al. Natural inorganic ingredients in wound healing. *Curr Pharm Des*. 2020;26:621–641.

11. Phull QZ, Arain AA, Ansari MA, Memon AR. Wound healing effects of bentonite: a rabbit model experimental study. *Biomed J*. 2018;10:7683–7686.

12. Sandri G, Aguzzi C, Rossi S, et al. Halloysite and chitosan oligosaccharide nanocomposite for wound healing. *Acta Biomater*. 2017;57:216–224. doi:10.1016/j.actbio.2017.05.032

13. Mohebali A, Abdouss M. Layered biocompatible pH-responsive antibacterial composite film based on HNT/PLGA/chitosan for controlled release of minocycline as burn wound dressing. *Int J Biol Macromol*. 2020;164:4193–4204.

14. Askari M, Afshar M, Naghizadeh A, Khorashadizadeh M, Zardast M. Bentonite nanoparticles and honey co-administration effects on skin wound healing: experimental study in the BALB/c MICE. *Int J Low Extrem Wounds*. 2022;2022:15347346221118497.

15. Wali A, Gorain M, Inamdar S, Kundu G, Badiger M. In vivo wound healing performance of halloysite clay and gentamicin-incorporated cellulose ether-PVA electrospun nanofiber mats. *ACS Appl Bio Mater*. 2019;2:4324–4334. doi:10.1021/acsabm.9b00589

16. Same S, Nakhjavani SA, Samee G, Davaran S, Jahanbani Y, Davaran S. Halloysite clay nanotube in regenerative medicine for tissue and wound healing. *Ceram Int*. 2022;48:31065–31079. doi:10.1016/j.ceramint.2022.05.037

17. Kurnik M, Ortega G, Dauphin-Ducharme P, Li H, Caceres A, Plaxco KW. Quantitative measurements of protein− surface interaction thermo-dynamics. *Proc Natl Acad Sci*. 2018;115:8352–8357. doi:10.1073/pnas.1800287115

18. Frutiger A, Tanno A, Hwu S, Tiefenauer RF, Voros J, Nakatsuka N. Nonspecific binding—fundamental concepts and consequences for biosensing applications. *Chem Rev*. 2021;121:8095–8160. doi:10.1021/acs.chemrev.1c00044

19. Castner DG. Biomedical surface analysis: evolution and future directions. *Biointerphases*. 2017;12:02C301. doi:10.1116/1.4982169

20. Rubio C, Costa D, Bellon-Fontaine MN, Relkin P, Pradier CM, Marcus P. Characterization of bovine serum albumin adsorption on chromium and AISI 304 stainless steel, consequences for the Pseudomonas fragi K1 adhesion. *Colloids Surf B*. 2002;24:193–205. doi:10.1016/S0927-7765(01)00242-9

21. Allizond V, Banche G, Salvoni M, et al. Facile one-step electrospinning process to prepare AgNPs-Loaded PLA and PLA/PEO mats with antibacterial activity. *Polymers*. 2023;15:1470. doi:10.3390/polym15061470

22. Comini S, Sparti R, Coppola B, et al. Novel silver-functionalized poly(ε-Caprolactone)/biphasic calcium phosphate scaffolds designed to counteract post-surgical infections in orthopedic applications. *Int J Mol Sci*. 2021;22:10176. doi:10.3390/ijms221810176

23. Qi X, Su T, Zhang M, et al. Sustainable, flexible and biocompatible hydrogels derived from microbial polysaccharides with tailorable structures for tissue engineering. *Carbohydr Polym*. 2020;237:116160. doi:10.1016/j.carbpol.2020.116160

24. Qi X, Su T, Zhang M, et al. Macroporous hydrogel scaffolds with tunable physicochemical properties for tissue engineering constructed using renewable polysaccharides. *ACS Appl Mater Interfaces*. 2020;12:13256–13264. doi:10.1021/acsami.9b20794

25. Su T, Zhang M, Zeng Q, et al. Mussel-inspired agarose hydrogel scaffolds for skin tissue engineering. *Bioact. Mater*. 2021;6:579–588. doi:10.1016/j.bioactmat.2020.09.004

26. Sandri G, Rossi S, Bonferoni MC, et al. Chitosan/glycosaminoglycan scaffolds for skin reparation. *Carbohydr Polym*. 2019;220:219–227. doi:10.1016/j.carbpol.2019.05.069

27. Sandri G, Miele D, Faccendini A, et al. Chitosan/glycosaminoglycan scaffolds: the role of silver nanoparticles to control microbial infections in wound healing. *Polymers*. 2019;11:1207. doi:10.3390/polym11071207

28. Ruggeri M, Sánchez-Espejo R, Casula L, et al. Clay-based hydrogels as drug delivery vehicles of curcumin nanocrystals for topical application. *Pharmaceutics*. 2022;14:2836. doi:10.3390/pharmaceutics14122836

29. Ruggeri M, Sánchez-Espejo R, Casula L, et al. Bentonite- and palygorskite-based gels for topical drug delivery applications. *Pharmaceutics*. 2023;15:1253. doi:10.3390/pharmaceutics15041253

30. Faccendini A, Ruggeri M, Miele D, et al. Norfloxacin-loaded electrospun scaffolds: montmorillonite nanocomposite vs. free drug. *Pharmaceutics*. 2020;12:325. doi:10.3390/pharmaceutics12040325

31. García-Villén F, Faccendini A, Aguzzi C, et al. Montmorillonite-norfloxacin nanocomposite intended for healing of infected wounds. *Int J Nanomedicine*. 2019;14:5051–5060. doi:10.2147/IJN.S208713

32. Sandri G, Faccendini A, Longo M, et al. Halloysite- and montmorillonite-loaded scaffolds as enhancers of chronic wound healing. *Pharmaceutics*. 2020;12:179. doi:10.3390/pharmaceutics12020179

33. Nordtveit RJ, Varum KM, Smidsrod O. Degradation of fully water-soluble, partially N-acetylated chitosans with lysozyme. *Carbohydr Polym*. 1994;23:253–260. doi:10.1016/0144-8617(94)90187-2

34. Kupiec TC, Matthews P, Ahmad R. Dry-heat sterilization of parenteral oil vehicles. *Int J Pharm Compd*. 2000;4:223–224.

35. Richard D, Ferrand M, Kearley GJ. LAMP, Large Array Manipulation Program, 1996 (2001 version). *J Neutron Res*. 1996;4:33–39. doi:10.1080/10238169608200065

36. Ruggeri M, Vigani B, Boselli C, et al. Smart nano-in-microparticles to tackle bacterial infections in skin tissue engineering. *Mater Today Bio*. 2022;16:100418. doi:10.1016/j.mtbio.2022.100418

37. Ruggeri M, Bianchi E, Rossi S, et al. Maltodextrin-amino acids electrospun scaffolds cross-linked with Maillard-type reaction for skin tissue engineering. *Biomater Adv*. 2022;133:112593. doi:10.1016/j.msec.2021.112593

38. Budai-Szűcs M, Ruggeri M, Faccendini A, et al. Electrospun scaffolds in periodontal wound healing. *Polymers*. 2021;13:307. doi:10.3390/polym13020307

39. Feng F, Liu Y, Zhao B, Hu K. Characterization of half N-acetylated chitosan powders and films. *Proced Engin*. 2012;27:718–732. doi:10.1016/j.proeng.2011.12.511

40. Hokputsa S, Hu C, Paulsen BS, Harding SE. A physico-chemical comparative study on extracellular carbohydrate polymers from five desert algae. *Carbohydr Polym*. 2003;54:27–32. doi:10.1016/S0144-8617(03)00136-X

41. Madejová J, Bujdák J, Janek M, Komadel P. Comparative FT-IR study of structural modifications during acid treatment of dioctahedral smectites and hectorite. *Spectrochim Acta A Mol Biomol Spectrosc*. 1998;54:1397–1406. doi:10.1016/S1386-1425(98)00040-7

42. Massaro M, Viseras C, Cavallaro G, et al. Synthesis and characterization of nanomaterial based on halloysite and hectorite clay minerals covalently bridged. *Nanomaterials*. 2021;11:506. doi:10.3390/nano11020506

43. Danková Z, Mockovčiaková A, Dolinská S. Influence of ultrasound irradiation on cadmium cations adsorption by montmorillonite. *Desalin Water Treat*. 2014;52:5462–5469. doi:10.1080/19443994.2013.814006

44. Faccendini A, Bianchi E, Ruggeri M, et al. Smart device for biologically enhanced functional regeneration of osteo–tendon interface. *Pharmaceutics*. 2021;13:1996. doi:10.3390/pharmaceutics13121996

45. Bochicchio D, Cantu L, Cadario MV, et al. Polystyrene perturbs the structure, dynamics, and mechanical properties of DPPC membranes: an experimental and computational study. *JCIS*. 2022;605:110–119.

46. Zaccai G. How soft is a protein? A protein dynamics force constant measured by neutron scattering. *Science*. 2000;288:1604–1607. doi:10.1126/science.288.5471.1604

47. Yan H, Zhang Z. Effect and mechanism of cation species on the gel properties of montmorillonite. *Colloids Surf A*. 2021;611:125824. doi:10.1016/j.colsurfa.2020.125824

48. García-Villén F, Sánchez-Espejo R, Borrego-Sánchez A, et al. Assessment of hectorite/spring water hydrogels as wound healing products. *Multidiscip Digital Publishing Inst Proc*. 2020;78:6.

49. Zheng Y, Zaoui A. Wetting and nanodroplet contact angle of the clay 2:1 surface: the case of Na-montmorillonite (001). *Appl Surf Sci*. 2017;396:717–722. doi:10.1016/j.apsusc.2016.11.015

50. Yang Y, Chen J, Ma G, et al. Waterborne cross-linkable polyacrylate latex coatings with good water resistance and strength stabilized by modified hectorite. *Polymers*. 2021;13:2470. doi:10.3390/polym13152470

51. Yi H, Jia F, Zhao Y, et al. Surface wettability of montmorillonite (0 0 1) surface as affected by surface charge and exchangeable cations: a molecular dynamic study. *Appl Surf Sci*. 2018;59:148–154. doi:10.1016/j.apsusc.2018.07.216

52. Zhang J, Zhou CH, Petit S, et al. Hectorite: synthesis, modification, assembly, and applications. *Appl Clay Sci*. 2019;177:114–138. doi:10.1016/j.clay.2019.05.001

53. Mohammed I, Al Shehri D, Mahmoud M, et al. A surface charge approach to investigating the influence of oil contacting clay minerals on wettability alteration. *ACS omega*. 2021;6:12841–12852. doi:10.1021/acsomega.1c01221

54. Bourlinos AB, Jiang DD, Giannelis EP. Clay−Organosiloxane hybrids: a route to cross-linked clay particles and clay monoliths. *Chem Mater*. 2004;16(12):2404–2410. doi:10.1021/cm049975z

55. Wilson CJ, Clegg RE, Leavesley DI, et al. Mediation of biomaterial–cell interactions by adsorbed proteins: a review. *Tissue Engin*. 2005;11:11–18. doi:10.1089/ten.2005.11.1

56. Mucha M, Maršálek R, Bukáčková M, Zelenková G. Interaction among clays and bovine serum albumin. *RSC Advan*. 2020;10:43927–43939. doi:10.1039/D0RA01430C

57. Wyrzykowski D, Hebanowska E, Nowak-Wiczk G, Makowski M, Chmurzyński L. Thermal behaviour of citric acid and isomeric aconitic acids. *J Therm Anal Calorim*. 2011;104:731–735. doi:10.1007/s10973-010-1015-2

58. Ng KW, Tham W, Lim TC, Werner Hutmacher D. Assimilating cell sheets and hybrid scaffolds for dermal tissue engineering. *J Biomed Mater Res A*. 2005;75:425–438. doi:10.1002/jbm.a.30454

59. Wang Y, Wang G, Luo X, Qiu J, Tang C. Substrate stiffness regulates the proliferation, migration, and differentiation of epidermal cells. *Burns*. 2012;38(3):414–420. doi:10.1016/j.burns.2011.09.002